PCCP

ROYAL SOCIETY OF CHEMISTRY

PAPER

View Article Online
View Journal | View Issue

Cite this: *Phys. Chem. Chem. Phys.*, 2021, **23**, 273

Quantum electronic control on chemical activation of methane by collision with spin–orbit state selected vanadium cation

Cheuk-Yiu Ng, *[a] Yuntao Xu, [a] Yih-Chung Chang, [a] Anna Wannenmacher,[a] Matthew Parziale[a] and P. B. Armentrout[b]

By coupling a newly developed quantum-electronic-state-selected supersonically cooled vanadium cation (V^+) beam source with a double quadrupole-double octopole (DQDO) ion–molecule reaction apparatus, we have investigated detailed absolute integral cross sections (σ's) for the reactions, $V^+[a^5D_J$ (J = 0, 2), a^5F_J (J = 1, 2), and a^3F_J (J = 2, 3)] + CH_4, covering the center-of-mass collision energy range of E_{cm} = 0.1–10.0 eV. Three product channels, VH^+ + CH_3, VCH_2^+ + H_2, and VCH_3^+ + H, are unambiguously identified based on E_{cm}-threshold measurements. No J-dependences for the σ curves (σ *versus* E_{cm} plots) of individual electronic states are discernible, which may indicate that the spin–orbit coupling is weak and has little effect on chemical reactivity. For all three product channels, the maximum σ values for the triplet a^3F_J state [$\sigma(a^3F_J)$] are found to be more than ten times larger than those for the quintet $\sigma(a^5D_J)$ and $\sigma(a^5F_J)$ states, showing that a reaction mechanism favoring the conservation of total electron spin. Without performing a detailed theoretical study, we have tentatively interpreted that a weak quintet-to-triplet spin crossing is operative for the activation reaction. The $\sigma(a^5D_0$, a^5F_1, and $a^3F_2)$ measurements for the VH^+, VCH_2^+, and VCH_3^+ product ion channels along with accounting of the kinetic energy distribution due to the thermal broadening effect for CH_4 have allowed the determination of the 0 K bond dissociation energies: $D_0(V^+–H)$ = 2.02 (0.05) eV, $D_0(V^+–CH_2)$ = 3.40 (0.07) eV, and $D_0(V^+–CH_3)$ = 2.07 (0.09) eV. Detailed branching ratios of product ion channels for the titled reaction have also been reported. Excellent simulations of the σ curves obtained previously for V^+ generated by surface ionization at 1800–2200 K can be achieved by the linear combination of the $\sigma(a^5D_J$, a^5F_J, and $a^3F_J)$ curves weighted by the corresponding Boltzmann populations of the electronic states. In addition to serving as a strong validation of the thermal equilibrium assumption for the populations of the V^+ electronic states in the hot filament ionization source, the agreement between these results also confirmed that the $V^+(a^5D_J$, a^5F_J, and $a^3F_J)$ states prepared in this experiment are in single spin–orbit states with 100% purity.

Received 15th August 2020,
Accepted 12th November 2020

DOI: 10.1039/d0cp04333h

rsc.li/pccp

I. Introduction

Methane (CH_4) is the simplest and most widespread alkane on earth. As the main component of natural gas that has been used as a combustion fuel, CH_4 is also one of the main non-CO_2 green-house gases, which is reported to be about 30 times more potent than CO_2 in the measure of global warming potential.[1] In addition, CH_4 is found on other planets and satellites in the solar system,[2,3] such as Mars and Titan; and CH_4 clathrates are one of the important carbon-containing ices in comets, interstellar space, and outer solar systems.[4,5]

As one of the four main C1 molecules on earth,[6] CH_4 has been proposed as a useful chemical feedstock to produce more-valued chemical species and intermediates, including methylene radical (CH_2) and methanol molecule (CH_3OH). Nevertheless, the activation and oxygenation of the C–H bond of CH_4 have been categorized as one of the "Holy Grails" in chemistry,[7] Due to its notorious thermodynamic stability and chemical inertness, the understanding of detailed mechanisms for chemical activation and functionalization of CH_4 remains far from completion.[8,9] Currently, large scale applications of CH_4 in industry have mainly been concerned with the conversion of CH_4 to H_2, which can then be used for the synthesis of straight-chain hydrocarbons *via* the Fischer–Tropsch process,[10,11] However, this method is highly energy intensive and thus expensive, making the development of new pathways for CH_4 activation with lower costs extremely desirable.

For decades, transition metal (TM) cations have been shown to exhibit very promising unique effects on activation of hydrocarbons including CH_4.[12–15] As early as in 1979, TM cations were reported to efficiently cleave alkanes by breaking the C–C and C–H

[a] *Department of Chemistry, University of California, Davis, CA 95616, USA. E-mail: cyng@ucdavis.edu*
[b] *Department of Chemistry, University of Utah, Salt Lake City, UT 84112, USA*

bonds.[16] Since then, a great wealth of both experimental and theoretical works on CH_4 activation have been published; and some summaries of these studies can be found in ref. 13, 15 and 17 The research of CH_4 activation has attracted good attention because it is a prototypical system for alkane activation as well as being abundant on earth.[18]

In 1987, the Armentrout group reported a heroic experiment concerning chemical reactivity dependences upon translational and electronic energy for the $V^+ + CH_4$ reaction using a guided ion beam (GIB) tandem mass spectrometer.[19] The effects of electronic energy were probed by varying the ion source conditions, such as the temperature (T) of the hot surface ionization (SI) filament and the electron ionization energy of the electron ionizer. However, due to the lack of energy resolution and the state-specific detection method, quantitative absolute integral cross section (σ) measurements for individual V^+ spin–orbit electronic states were not achieved, although approximate state-specific σ determinations were made. Nevertheless, based on observations of the GIB experiment, it was suggested that the mechanism for the activation of CH_4 by V^+ preferentially proceeds through a triplet spin V^+ inserted $[H–V^+–CH_3]$ intermediate, favoring the conservation of total electron spin.

In 1997, the Brucat group reported a photodissociation study of V^+CH_4 ion–molecule complexes formed in a laser-driven-plasma supersonic beam source.[20] The majority of complexes thus formed was believed to have the structure of the charge-induced dipole ion–molecule complex $[V^+–CH_4]$. However, the authors could not preclude the existence of a minor amount with the structure of the V^+ inserted $[H–V^+–CH_3]$ intermediate.

A density functional (DFT) theoretical study was later performed for the $V^+ + CH_4$ reaction system by Sicilia and Russo in 2002, which has provided some valuable insights into the activation mechanism,[21] and agreed with the qualitative potential energy surface originally suggested by Aristov and Armentrout.[19] The DFT calculation suggested that three reaction intermediates may be formed along the reaction coordinates: the first one is the ion-induced-dipole complex $[V^+–CH_4]$, which may evolve to the inserted intermediate $[H–V^+–CH_3]$. This second intermediate, in which the C–H bond of CH_4 has been activated, was expected to lead to the formation of VH^+ and VCH_3^+. The last intermediate may be the $[H_2–V^+–CH_2]$ structure formed *via* rearrangement of the other two intermediates, leading to the formation of the $VCH_2^+ + H_2$ product channel. The mechanism, invoking the conservation of total electron spins, is also revealed in the DFT theoretical study.

In 2009, the Bohme group reported a systematic kinetic study on the reactions between CH_4 and 59 atomic metal cations, which included the V^+ ion at room temperature prepared by using a plasma selected ion flow tube tandem mass spectrometer.[17] In these reactions, internal excitations of the reactant TM cations were supposed to be quenched down to the ground state by collisions with the carrier gas, such as helium. However, the authors admitted that the exact electronic states and the relative populations of the reactant TM ions after the collisions are uncertain. This may due to different relaxation mechanisms involved for different long-lived electronically excited TM ions.[22–24] To the best of our knowledge, no σ measurements with reactant V^+ ions prepared in single electronic states, especially in excited V^+ states, have been reported previously for the $V^+ + CH_4$ reaction. The successful search of quantum electronic state controls of chemical reactivity of V^+ ion in its excited electronic states is expected to promote new reaction pathways of catalytic relevance.

Recently, we have developed a two-color visible-ultraviolet (VIS-UV) laser pulsed field ionization-photoion (PFI-PI) detection method, which can be used to prepare V^+ ions in 13 different spin–orbit coupled electronic states, a^5D_J (J = 0–4), a^5F_J (J = 1–5), and a^3F_J (J = 2–4), with high laboratory kinetic energy (E_{lab}) resolution or narrow ΔE_{lab} spread for V^+ ion. This development has made possible systematic chemical reactivity measurements of quantum state-selected V^+ ions with simple atmospheric gases.[25] Combining the VIS-UV laser PFI-PI ion source with the double quadrupole-double octopole (DQDO) ion–molecule reaction apparatus, we have previously investigated detailed chemical reactivity of V^+ ion by activating CO_2, D_2 and O_2 as a function of electronic state and kinetic energy of V^+ ion.[24,26,27] The main observation of these latter experiments is that the triplet electronic states ($a^3F_{2–4}$) are much more reactive in activating CO_2 and D_2 than the other two quintet electronic states, in agreement with the more qualitative determinations of the Armentrout group on the same systems.[23,28] No J dependences are observed for the σ values of individual $V^+[a^5D_J$ (J = 0, 2), a^5F_J (J = 1, 2), and a^3F_J (J = 2, 3)] electronic states to CO_2 and D_2 activation reaction, while the J-state effect for the $V^+(a^3F_{2,3}) + O_2$ reactions are unambiguously identified,[29] where J is the total angular momentum quantum number of the spin–orbit state of V^+ ion. Furthermore, the σ curves (σ *versus* E_{cm} plots) observed show that both electronic and E_{cm} energies of the reaction can effectively couple with the reaction coordinates, allowing the E_{cm}-threshold measurements to yield reliable thermochemical properties, such as 0 K bond dissociation energies (D_0's) and heats of formation ($\Delta_f H_0$'s) for TM containing molecular species, many of which are still unavailable in the literature. To examine whether the dominant reaction mechanism observed in the $V^+ + D_2(CO_2)$ reaction systems is also valid for the $V^+ + CH_4$ reaction is a major motivation of the present quantum electronic state selected study.

Here, we present the σ values for the $V^+ + CH_4$ reaction when V^+ ions are prepared into single spin–orbit electronic states, covering the E_{cm} range from 0.1 to 10.0 eV. Detailed dependences of the spin–orbit electronic states and the E_{cm} on σ values and product branching ratios (BR's) have also been investigated in the present study for the first time. Since the two-color VIS-UV laser PFI-PI method is readily applicable to other TM cation species, this work can also be considered as a demonstration experiment, illustrating that chemical reactivity of TM ions toward hydrocarbons can be readily examined experimentally with TM ions prepared in single, pure electronic states, one spin–orbit state at a time. Thus, the results of this study would serve as a guiding experiment for future state-selected ion–molecule reaction studies involving other TM cations.

II. Experimental considerations

Since the detailed arrangement of the two-color VIS-UV laser PFI-PI ion source and procedures used for σ measurements

employing the DQDO ion–molecule reaction apparatus have been reported previously,[24,25,30,31] only a brief description is given below.

(a) Two-color VIS-UV laser PFI-PI ion source

The VIS-UV laser PFI-PI detection scheme has been recently developed in our group to prepare gaseous V^+ ions in one of the thirteen quantum spin–orbit electronic states: a^5D_J (J = 0–4), a^5F_J (J = 1–5), and a^3F_J (J = 2–4) in the form of a pulsed supersonic beam, achieving E_{cm} values down to thermal energies. The precursor neutral V atom sample, in the form of a pulsed (30 Hz) supersonically cooled atomic beam, is generated by a Smalley-type pulsed laser ablation TM beam source. The laser system used for photo-exciting the neutral V atoms consists of two independently tunable dye lasers pumped by one pulsed Nd:YAG laser operated at 30 Hz. The first dye laser is pumped by the third harmonics of the Nd:YAG laser to generate the VIS output (ω_1). The second dye laser is pumped by the second or third harmonics of the same Nd:YAG laser to provide the UV output (ω_2) after passing through a frequency doubling crystal. The VIS ω_1 and UV ω_2 laser beams are then merged into the photoexcitation (PEX) region by using a dichroic mirror. The VIS and UV laser beams perpendicularly intersect the neutral V atom sample in the form of a supersonically cooled V/He seeded beam. The VIS ω_1 is fixed to excite the neutral V atoms from the ground state to a selected neutral intermediate state, and the UV ω_2 is tunable such that the total photoexcitation frequency of (ω_1 + ω_2) covers the photoexcitation transition frequencies needed for photoionization from the ground state to the spin–orbit electronic states of interest. High-n ($n > 60$) Rydberg states of V [V*(n)] converging to the ionic states of interest are ionized by PFI to produce PFI-PIs in one of the V^+ [a^5D_J (J = 0–4), a^5F_J (J = 1–5), and a^3F_J (J = 2–4)] spin–orbit J-states.

Because prompt ions without pure state selection can also be produced along with PFI-PI formation, the most important issue is to reject prompt ions from the PFI-PI beam, and this is achieved as described in detail elsewhere.[24–26,30,31] Readers are referred to the two-color laser PFI-PI spectra for $V^+[a^5D_J$ (J = 0–4)], $V^+[a^5F_J$ (J = 1–5)], and $V^+[a^3F_J$ (J = 2–4)] shown in Fig. 8(a), (b), and (c) of ref. 25, respectively. The fully J-resolved PFI-PI spectra observed indicate that the preparation of V^+ ion in single quantum spin–orbit electronic states is well achieved.

(b) DQDO ion–molecule reaction apparatus and σ measurements

The DQDO ion–molecule reaction apparatus consists of, in sequential order, a supersonically cooled V atom source produced by pulsed laser ablation of a rotating and translating V-rod, a reactant quadrupole mass filter (QMF), a reaction gas cell situated between two radio frequency (rf)-octopole ion guides, a product QMF, and a Daly-type ion detector.[32] The second harmonic output of an Nd:YAG laser operated at 2 mJ and 30 Hz is employed as the ablation laser. The V gaseous plumes formed by ablation are merged into a He gas flow, forming a V/He seeded beam. Cooling of the V atom sample occurs as the V/He seeded gas undergoes supersonic expansion. Charged species, which are also formed by laser ablation, are deflected away from the V/He beam path by a pair of ion repeller plates biased at a sufficiently high DC electric field. In this experiment, the reactant QMF is only used as an ion lens. The dual set of rf-octopoles can be used to extract slow product ions formed inside the gas cell and maintain high ion transmission through the gas cell by applying a small dc field between the two rf-octopoles. The gas cell is connected with an electromagnetic valve for gas filing; and the gas cell pressure is monitored by an MKS Baratron. In this study, the pressure of CH_4 in the gas cell is maintained at (1.0 or 2.0) $\times 10^{-4}$ torr, which is low enough to satisfy the thin target conditions.[33,34] The product QMF and the modified Daly-type detector form the detection system for reactant and product ions.

The σ measurement involves the determination of intensities of the reactant and products ions. Based on the thin target ion-neutral scattering scheme, the σ value can be deduced as $[(kT)/(Pl)][\ln((I + i)/I)]$, where k, T, P, l, I, and i represent the Boltzmann constant, the temperature and the pressure of the neutral reactant in the reactant gas cell, the effective length of the gas cell, the intensity of the unreacted reactant V^+ ions, and the intensity of the product ions, respectively. Under the thin target conditions, product ions formed by secondary reactions are negligible. All σ curves shown in this work are the averaged results of at least three independent measurements. The run-to-run uncertainties are found in the range of 5–10% and the absolute uncertainties of σ's determined in this work are estimated to be $\leq$30%.

The E_{cm} is converted from the laboratory kinetic energy (E_{lab}) by using the formula $E_{cm} = E_{lab}\,[M/(m^+ + M)]$, where m^+ and M represent the masses of V^+ ion and CH_4 molecule, respectively. As pointed out previously, the thermal motion of neutral CH_4 molecules inside the gas cell can give rise to the kinetic energy distribution, which is referred to here as the ''thermal broadening'' effect. This distribution can significantly affect the E_{cm} spread or ΔE_{cm} resolution.[35] Thus, for energetic measurements, such as bond dissociation energies (D_0's) deduced in the studies of the $V^+ + D_2$ (CO_2, CH_4) reactions, we have taken into account the kinetic energy distribution as described below.

III. Results and discussions

(a) Mass spectra

The mass spectra for the quantum spin–orbit electronic state-selected $V^+(a^3F_2)$ ion source and the $V^+(a^3F_2) + CH_4$ reaction are shown as the black curves in Fig. 1(a) and (b), respectively. For both mass spectra, E_{cm} was set at 2.0 eV. To better view the weak mass peaks with low intensities, the original mass spectra in black are magnified by a factor of 15. The magnified mass spectra thus obtained are shown in red. As shown in Fig. 1(a), the three ion peaks observed at the mass to charge ratios of m/z = 50, 51, and 67 can readily be assigned as $^{50}V^+$, $^{51}V^+$, and VO^+, respectively. We note that the intensity ratio of the mass peaks for $^{50}V^+$ and $^{51}V^+$ are found to be consistent with the known natural abundances of the V^+ isotopes.[36] Since this mass spectrum for the $V^+(a^3F_2)$ ion source was recorded without CH_4 in the reaction gas cell, all the ion peaks, except the one for $^{51}V^+$, can be considered as background ions.

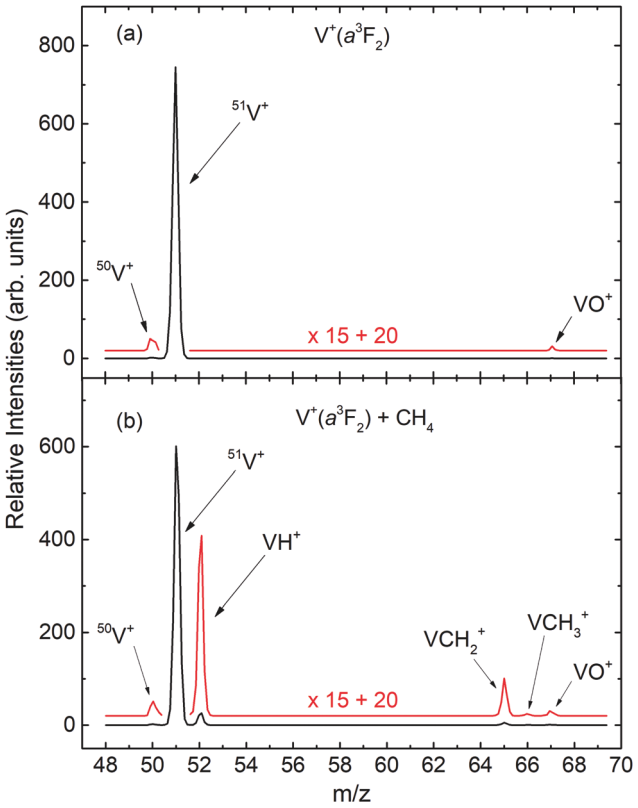

Fig. 1 Comparison of mass spectra recorded with and without reactant CH_4 gas in the reaction gas cell. (a) Mass spectrum of the $V^+(a^3F_2)$ state-selected PFI-PI ion source recorded without CH_4 in the gas cell. (b) Mass spectrum of the $V^+(a^3F_2)$ + CH_4 state-selected reaction with CH_4 in the gas cell. For both spectra, the E_{cm} is set to 2.0 eV.

Different from the spectrum of Fig. 1(a), the mass spectrum in Fig. 1(b) exhibits six ion peaks at m/z = 50, 51, 52, 65, 66, and 67, which are marked in Fig. 1(b) as $^{50}V^+$, $^{51}V^+$, VH^+, VCH_2^+, VCH_3^+, and VO^+, respectively. We find that the intensity of the m/z = 67 (assigned as VO^+) peak of Fig. 1(b) is very similar to that of Fig. 1(a), consistent with its formation from reactions of V^+ with trace amounts of O_2 or H_2O, where the reactions occur with near unit efficiency.[29] Since the m/z values for VO^+ and VCH_4^+ are identical, this observation can be taken as evidence that negligible VCH_4^+ ion–molecule complexes are formed by multiple collision events in the reaction gas cell. The mass spectrum of Fig. 1(b) also shows no evidence for the formation of VCH^+ ion. Similar observations were also obtained from the mass spectra recorded with V^+ ion prepared in different electronic states at different E_{cm} values. Therefore, we can conclude that VH^+, VCH_2^+, and VCH_3^+ ions are identified as the major primary product ions in the present experiment. However, this observation cannot exclude the formation of VCH^+ ion. Based on σ measurements presented below, if VCH^+ is formed, we estimate its σ value to be about $\leq$0.001 Å^2.

The reaction product channels or states associated with the formation of product ions are listed in reactions (1)–(3), along with the corresponding apparent threshold energies of reaction (E_T) observed here at the reactant sample temperature T, which is mostly determined by the thermal energy of neutral methane in this case but also includes the minor ion kinetic energy distribution.

$$V^+(a^5D_0) + CH_4(X^1A_1) \rightarrow VH^+(X^4\Delta) + CH_3(X^2A_2'') \quad E_T = 1.9 \pm 0.1 \text{ eV} \quad (1)$$

$$V^+(a^5D_0) + CH_4(X^1A_1) \rightarrow VCH_2^+(X^3A_1) + H_2(X^1\Sigma_g^+) \quad E_T = 1.2 \pm 0.1 \text{ eV} \quad (2)$$

$$V^+(a^5D_0) + CH_4(X^1A_1) \rightarrow VCH_3^+(X^4B_1) + H(^2S_{1/2}) \quad E_T = 1.8 \pm 0.1 \text{ eV} \quad (3)$$

The E_T values for these reactions given above are obtained directly or indirectly by the E_{cm}-threshold measurements, in which the T is not zero. We note that the E_{cm}-thresholds marked in Fig. 2(a)–(f) are identical with their corresponding E_T values. Reactions (1)–(3) are all endothermic with positive E_T values. Since the $V^+(a^5D_0)$ + $CH_4(X^1A_1)$ reactant state is the ground electronic state, it is convenient to use it as the reference state of this reaction system. The E_T's for these reaction product channels with V^+ ions prepared in the excited electronic states, *i.e.*, $V^+(a^5F_1)$ or $V^+(a^3F_2)$, can be obtained readily by subtracting the known electronic energy of the excited reactant V^+ ion[25,37] from the E_T's for reactions (1)–(3) with V^+ ion prepared in the a^5D_0 ground electronic state. Here, the σ values for reactions (1), (2), and (3) are designated as $\sigma(a^5D_0$: $VH^+)$, $\sigma(a^5D_0$: $VCH_2^+)$, and $\sigma(a^5D_0$: $VCH_3^+)$, respectively.

Because of the very low $\sigma(a^5D_0$: $VCH_3^+)$ and $\sigma(a^5F_1$: $VCH_3^+)$ values, the E_{cm}-thresholds for these σ curves cannot be determined with high precision. However, a more precise E_{cm}-threshold for $\sigma(a^5D_0$: $VCH_3^+)$ can be determined by adding the electronic energy of 1.1 eV for $\sigma(a^3F_2$: $VCH_3^+)$ to the measured E_{cm}-threshold of 0.7 ± 0.1 eV for $\sigma(a^3F_2$: $VCH_3^+)$, yielding a E_{cm}-threshold value of 1.8 ± 0.1 eV for the $\sigma(a^5D_0$: $VCH_3^+)$. This value thus obtained is in marginal agreement with the directly measured E_{cm}-threshold of 3.0 ± 1.0 eV for the $\sigma(a^5D_0$: $VCH_3^+)$, after taking into account of the experimental uncertainties. We note that the large E_{cm} step size (1 eV) used for recording the latter spectrum makes it undesirable for use of precise energetic deductions.

On the basis of the $\sigma(a^5F_1$: $VCH_2^+)$ measurements of Fig. 2(e), the detection sensitivity of the instrument for σ measurements used is estimated to be 0.001 Å^2 for $\sigma(VCH^+)$. Although this experiment cannot exclude VCH^+ as a primary product ion, if it is formed, $\sigma(VCH^+)$ is expected to be $\leq$0.001 Å^2. As mentioned above, the pressure of CH_4 in the gas cell used in this work was controlled to sufficiently low values in order to minimize multiple-collision events.

(b) Quantum electronic state effects

The $\sigma(VH^+)$, $\sigma(VCH_2^+)$ and $\sigma(VCH_3^+)$ curves are depicted in Fig. 2(a)–(c), Fig. 2(d)–(f), and Fig. 2(g)–(h), respectively. The σ's for the $V^+(a^5D_0$, a^5F_1, and $a^3F_2)$ states are depicted with black circles, red squares, and blue triangles in Fig. 2(a)–(h). For $\sigma(VH^+)$, Fig. 2(a) shows the direct contrast when V^+ is prepared in the a^5D_0, a^5F_1, and a^3F_2 spin–orbit states, and

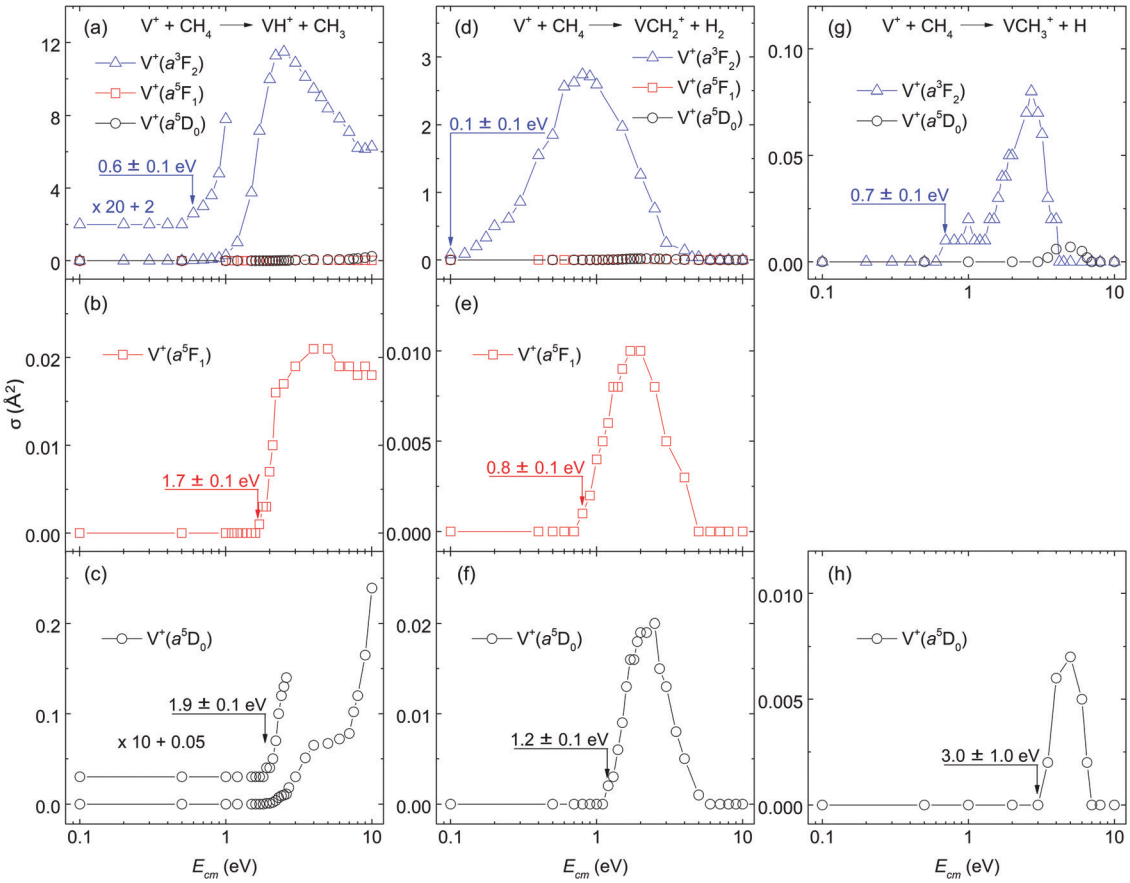

Fig. 2 Comparison of the $\sigma(VH^+)$, $\sigma(VCH_2^+)$, and $\sigma(VCH_3^+)$ for the reaction system of $V^+(a^3F_2, a^5F_1, \text{and } a^5D_0) + CH_4$. (a) shows the $\sigma(a^3F_2$: $VH^+)$, $\sigma(a^5F_1$: $VH^+)$, and $\sigma(a^5D_0$: $VH^+)$ in blue triangles, red squares, and black circles, respectively. (b) and (c) Depict the magnified view of the $\sigma(a^5F_1$: $VH^+)$ and $\sigma(a^5D_0$: $VH^+)$, respectively. Similarly, the $\sigma(VCH_2^+)$ and $\sigma(VCH_3^+)$ are shown in (d)–(f) and (g), (h), respectively. In order to better examine the E_{cm}-threshold positions, the $\sigma(a^3F_2$: $VH^+)$ is amplified by a factor of 20 in (a), and the $\sigma(a^5D_0$: $VH^+)$ is amplified by a factor of 10 in (c).

Fig. 2(b) and (c) provide a magnified view for $\sigma(a^5F_1$: $VH^+)$ and $\sigma(a^5D_0$: $VH^+)$, respectively. Similar comparisons for $\sigma(VCH_2^+)$ are made in Fig. 2(d) and (f), as well as for $\sigma(VCH_3^+)$ in Fig. 2(g) and (h). Since $\sigma(a^5F_1$: $VCH_3^+)$ was below the detection limit of ≈ 0.001 Å^2 in the E_{cm} range of interest, no $\sigma(a^5F_1$: $VCH_3^+)$ curve was recorded.

One of the major observations for quantum electronic state effects on chemical reactivity of the $V^+(a^3F_2, a^5F_1, \text{and } a^5D_0) + CH_4$ reaction system [as shown in Fig. 2(a)–(h)] is that the triplet reactant ion, $V^+(a^3F_2)$, is much more reactive than the quintet reactant ions, $V^+(a^5D_0)$ and $V^+(a^5F_1)$. Specifically, as depicted in Fig. 2(a), $\sigma(a^3F_2$: $VH^+)$ is dominantly higher than $\sigma(a^5D_0$: $VH^+)$ by 1000, 120, and 25 times at E_{cm} = 2.0, 5.0, and 10.0 eV, respectively. Similarly, in Fig. 2(d), $\sigma(a^3F_2$: $VCH_2^+)$ is higher than $\sigma(a^5D_0$: $VCH_2^+)$ by 65 and 12 times at E_{cm} = 2.0, and 5.0 eV, respectively; and in Fig. 2(g), the peak value of $\sigma(a^3F_2$: $VCH_3^+)$ is about 10 times higher than that of $\sigma(a^5D_0$: $VCH_3^+)$.

Chemical reactivity enhancement observed for the $V^+(a^3F_2) + CH_4$ reaction can be rationalized by the conservation rule of total electron spins.[19,21,24,26] The surmised reaction mechanisms are depicted in the schematic energy level diagram of Fig. 3. On the left side of Fig. 3, we show the three reactant states, $V^+(a^3F_2) + CH_4(X^1A_1)$ in red, and $V^+(a^5F_1) + CH_4(X^1A_1)$ and $V^+(a^5D_0) + CH_4(X^1A_1)$ states in black. The three product states, $VH^+(X^4\Delta) + CH_3(X^2A_2'')$, $VCH_3^+(X^4B_1) + H(^2S_{1/2})$, and $VCH_2^+(X^3A_1) + H_2(X^1\Sigma_g^+)$, identified in this experiment are shown on the right side of Fig. 3 according to their energy order. At higher energies, we also include in Fig. 3 the possible dissociative product channels, $V^+(a^5D_0) + CH_3(X^2A_2'') + H(^2S_{1/2})$ and $VCH_2^+(X^3A_1) + H(^2S_{1/2}) + H(^2S_{1/2})$. The lack of precise energetics has limited the inclusion of other possible product states in the energy level diagram. With the exception of the $VCH_2^+(X^3A_1) + H_2(X^1\Sigma_g^+)$ product state, which can only correlate adiabatically to triplet reactant states, the other product states of Fig. 3 are shown in blue, indicating that they can correlate to both triplet and quintet reactant states.

As suggested by the previous experimental results[19] and DFT calculations,[21] two kinds of reaction intermediates, $[V^+CH_4]$ and $[HVCH_3^+]$, are involved, and each intermediate can be formed in the triplet as well as quintet states. These intermediates are shown in the middle of the energy level diagram of Fig. 3 according to the DFT predictions and are highlighted in colors based on their multiplicities: red for triplet states and black for quintet states. Since the bond dissociation energy of V^+–H is much weaker than that of H–CH_3, the formation of the $[V^+CH_4]$ intermediate is not expected to lead to the cleavage of the C–H bond of CH_4. Thus, as depicted in Fig. 3, the

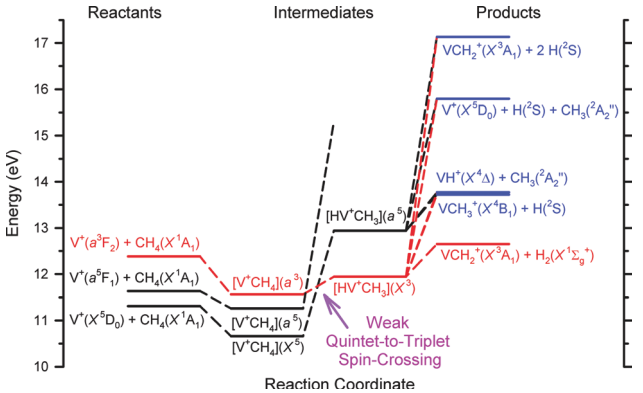

Fig. 3 Schematic energy level diagram of the surmised reaction mechanism for the $V^+ + CH_4$ reaction system, where the zero energy is set by the energy of the $V^+(a^5D_0)$ ground state. The colors of each component are based upon the total coupled electron spins or multiplicity: red for the triplet, black for the quintet, and purple for both the triplet and quintet. On the left side are the three reactant states, in the middle are the proposed reaction intermediates, and on the right side are the selected product channels. The main reaction mechanism of the $V^+ + CH_4$ reaction is interpreted here to favor the conservation of the total electron spins with a "weak quintet-to-triplet spin crossing", which is marked nominally by the purpled dashed arrow near the middle bottom of the figure. We note that the a^5F_J state does not correlate with the $[V^+CH_4](X^5)$ ground state, but rather with another excited state of this species still having quintet spin. This is shown in the potential energy surface in ref. 19. The purple arrow points to the crossing between the triplet and quintet dashed lines.

ion–molecule complex $[V^+CH_4]$ may proceed to rearrange forming the inserted $[HVCH_3^+]$ structure.

The key reaction intermediate proposed by the previous DFT calculation[21] has an inserted triplet $[HV^+CH_3](X^3)$ structure[19,21] at an energy lower than that of the $V^+(a^3F_2) + CH_4(X^1A_1)$ reactant state. Therefore, the $V^+(a^3F_2) + CH_4(X^1A_1)$ reactant state can form the inserted $[HV^+CH_3](X^3)$ intermediate *via* the $[V^+CH_4](a^3)$ ion–molecule complex without flipping electron spins because both of them are in reaction surfaces with the same multiplicity. Meanwhile, reactant states, $V^+(a^5D_0) + CH_4(X^1A_1)$ and $V^+(a^5F_1) + CH_4(X^1A_1)$, may form a quintet inserted intermediate $[HV^+CH_3](a^5)$ by conserving the total electron spins. Based on the previous experimental and theoretical work,[19,21] the $[HV^+CH_3](X^3)$ and $[HV^+CH_3](a^5)$ intermediates are estimated to be 0.6 and 1.6 eV, respectively, higher than the $V^+(a^5D_0) + CH_4(X^1A_1)$ ground reactant state. Meanwhile, $V^+(a^3F_2)$ is known to be about 1.1 eV higher than $V^+(a^5D_0)$. Thus, $V^+(a^3F_2) + CH_4(X^1A_1)$ is both exothermic (by 0.5 eV) and spin-allowed when forming the $[HV^+CH_3](X^3)$ intermediate. In contrast, both reactant states, $V^+(a^5D_0) + CH_4(X^1A_1)$ and $V^+(a^5F_1) + CH_4(X^1A_1)$, are endothermic and spin-forbidden when forming the $[HV^+CH_3](X^3)$ intermediate, which may lead to very low reactivity of $V^+(a^5D_0)$ and $V^+(a^5F_1)$ compared with $V^+(a^3F_2)$ towards the activation of CH_4 leading to $VCH_2^+ + H_2$. The "weak quintet-to-triplet spin crossing" region is marked nominally by the purple dashed arrow in the schematic energy level diagram of Fig. 3. The observation of the product state, $VCH_2^+(X^3A_1) + H_2(X^1\Sigma_g^+)$, of reaction (2) is a strong manifestation of the "weak electron spin crossing" mechanism. If the reaction of $V^+ + CH_4$ strictly follows a "no spin-crossing" reaction mechanism, the triplet product state, $VCH_2^+(X^3A_1) + H_2(X^1\Sigma_g^+)$, could not have been formed from the quintet reactant states, $V^+(a^5D_0) + CH_4(X^1A_1)$ and $V^+(a^5F_1) + CH_4(X^1A_1)$. We are grateful to a reviewer who has pointed out that the observed product distribution could be explained by a statistical analysis of the lifetime of the $V^+(CH_4)$ collision complex and the barriers involved for the relevant reaction steps. Because this theoretical analysis is beyond the scope of the present work, we hope that the results of this experiment will interest in such future theoretical studies. We note that at sufficiently high E_{cm} values, the collision complex dissociation model is likely to be invalid.

The observed E_{cm}-thresholds of 0.1 ± 0.1 eV for $\sigma(a^3F_2: VCH_2^+)$, 0.8 ± 0.1 eV for $\sigma(a^5F_1: VCH_2^+)$, and 1.2 ± 0.1 eV for $\sigma(a^5D_0: VCH_2^+)$ as shown in Fig. 2(d)–(f) are consistent with the electronic energies of 0.3 eV for $V^+(a^5F_1)$ and 1.1 eV for $V^+(a^3F_2)$ measured with respect to that for $V^+(a^5D_0)$.[38] The operation of a "weak quintet-to-triplet spin crossing" allows a very minor fraction of the quintet reactant states, $V^+(a^5D_0) + CH_4(X^1A_1)$ and $V^+(a^5F_1) + CH_4(X^1A_1)$, to "switch" to form the triplet $[HV^+CH_3](X^3)$ intermediate. Thus, the operation of this "weak quintet-to-triplet spin crossing" mechanism is consistent with the fact that both the $\sigma(a^5D_0: VCH_2^+)$ and $\sigma(a^5F_1: VCH_2^+)$ values are very small compared with the $\sigma(a^3F_2: VCH_2^+)$.

As shown in Fig. 2(a)–(f), the ground state $V^+(a^5D_0)$ ion is mildly more reactive with CH_4 than the first excited state $V^+(a^5F_1)$ ion, even though the latter has a 0.3 eV higher energy level. Similar reactivity behaviors have been observed in other reaction systems, such as the $V^+ + CO_2$ and $V^+ + D_2$ reactions.[24,26] As discussed previously, the high-spin coupled 4*s* electron of the $V^+(a^5F_1)$ ion is believed to adversely affect the bonding and chemical reactivity.[12,23] The 4s electron is speculated to generate larger repulsive interactions between the V^+ ion and CH_4 molecule than the 4d electrons when the two moieties approach each other; and the larger repulsive interaction leads to lower reaction probabilities. Notably, even though the $V^+(a^5F_1)$ with CH_4 reaction is less efficient than the other states, the E_{cm}-thresholds for endothermic reactions observed in the present study are consistent among all states. As shown in Fig. 2(b), (c), (e), and (f), the threshold positions for the reactant state of $V^+(a^5F_1) + CH_4(X^1A_1)$ is between 0.2 and 0.4 eV lower than that of $V^+(a^5D_0) + CH_4(X^1A_1)$, which is in accord with the relative energies of the two V^+ electronic states. This observation indicates that both the electronic energy of V^+ and the kinetic energy E_{cm} of the $V^+ + CH_4$ reaction can couple with the reaction coordinates to facilitate product ion formation. Furthermore, this observation also supports the conclusion that the reactant V^+ ions prepared in this experiment are in pure, single electronic states.

(c) Kinetic energy effects

Besides the quantum electronic state effects, the kinetic energy effects for the reaction system of $V^+ + CH_4$ can also be observed in Fig. 2(a)–(h). As shown in these figures, all the reaction product channels or states observed for this reaction system are endothermic, which is in agreement with the thermochemistry analysis as the electronic energies of V^+ are changed. For the $\sigma(VH^+)$ shown in Fig. 2(a)–(c), in order to display the threshold regions more clearly, the $\sigma(a^3F_2: VH^+)$ and $\sigma(a^5D_0: VH^+)$ curves are amplified by a factor of 20 and 10, respectively. As shown in Fig. 2(a)–(c), the $\sigma(a^3F_2: VH^+)$, $\sigma(a^5F_1: VH^+)$, and $\sigma(a^5D_0: VH^+)$ curves exhibit distinct

behaviors, indicating that the electronic states of V^+ ions play an important role in the formation of this reaction channel. Specifically, $\sigma(a^3F_2$: $VH^+)$ has a threshold near E_{cm} = 0.6 eV and then increases almost exponentially above the threshold. At E_{cm} = 2.5 eV, $\sigma(a^3F_2$: $VH^+)$ reaches the peak value of $\approx$11.5 Å^2. This σ value is quite high for an endothermic reaction, Above 2.5 eV, $\sigma(a^3F_2$: $VH^+)$ decreases almost exponentially until E_{cm} = 8.0 eV. At E_{cm} = 8.0–10.0 eV, the decreasing trend *versus* E_{cm} ends and even starts to increase mildly. Different from $\sigma(a^3F_2$: $VH^+)$, $\sigma(a^5F_1$: $VH^+)$ has a threshold at E_{cm} = 1.7 eV and then reaches a peak value of $\approx$0.02 Å^2 near E_{cm} = 3.0 eV. Above 3.0 eV, $\sigma(a^5F_1$: $VH^+)$ is almost flat. The $\sigma(a^5D_0$: $VH^+)$ shows similar profiles as that of $\sigma(a^5F_1$: $VH^+)$ when $E_{cm} \leq$ 3.0 eV except the threshold position is 1.9 eV. However, $\sigma(a^5D_0$: $VH^+)$ keeps increasing as E_{cm} further increases above 3.0 eV. As shown in Fig. 3, when E_{cm} is high enough to form the quintet $[HV^+CH_3](a^5)$ intermediate, it can lead to the formation of VH^+ and VCH_3^+ without "weak quintet-to-triplet spin crossing". Thus, $\sigma(VH^+)$ and $\sigma(VCH_3^+)$ are expected to be observed at high E_{cm} values. The trends of $\sigma(a^3F_2$: $VH^+)$, $\sigma(a^5F_1$: $VH^+)$, and $\sigma(a^5D_0$: $VH^+)$ curves shown in Fig. 2(a)–(c), suggest that these curves may consist of a higher and a lower E_{cm} overlapping components. As the electronic energy is decreased, the lower E_{cm} component is found to diminish, resulting in the domination of the higher E_{cm} component of $\sigma(a^5D_0$: $VH^+)$ curve as depicted in Fig. 2(c), To understand the dynamics features observed for the $\sigma(VH^+)$ as a function of E_{cm} and electronic state of V^+, rigorous theoretical dynamics calculations based on accurate reaction potential energy surfaces are required.

One different feature for $\sigma(VH^+)$ in Fig. 2(a)–(c) compared to $\sigma(VCH_2^+)$ in Fig. 2(d)–(f), and $\sigma(VCH_3^+)$ in Fig. 2(h) and (g) is that $\sigma(VH^+)$ remains high at E_{cm} ($\geq$4.0 eV) values. This observation could be the result of different reaction dynamics involved in the formation of different reaction product channels. At sufficiently high E_{cm} values ($\geq$4.482 eV), the collision-induced dissociation (CID) product channels, such as reaction (4), are expected to occur.

$$V^+(a^5D_0) + CH_4(X^1A_1) \rightarrow V^+(a^5D_0) + CH_3(X^2A_2'') + H(^2S_{1/2})$$
$$E_0 = 4.482 \pm 0.001 \text{ eV} \qquad (4)$$

The formation of the CID product channel in reaction (4) can also be considered as generated from the further dissociation of the excited VH^+ and/or VCH_3^+ ions initially produced in the collision of $V^+(a^5D_0) + CH_4(X^1A_1)$.

The E_{cm} dependences of $\sigma(VCH_2^+)$ are shown in Fig. 2(d)–(f). Similar to the $\sigma(VH^+)$, all three $\sigma(VCH_2^+)$ reaction channels are found to be endothermic. The E_{cm}-thresholds are observed at E_{cm} = 0.1 ± 0.1, 0.8 ± 0.1, and 1.2 ± 0.1 eV for $\sigma(a^3F_2$: $VCH_2^+)$, $\sigma(a^5F_1$: $VCH_2^+)$, and $\sigma(a^5D_0$: $VCH_2^+)$, respectively. The differences of these E_{cm}-thresholds observed are consistent with the electronic energies of the corresponding V^+ ions. The $\sigma(a^3F_2$: $VCH_2^+)$, $\sigma(a^5F_1$: $VCH_2^+)$, and $\sigma(a^5D_0$: $VCH_2^+)$ curves are found to have similar profiles exhibiting a single peak. The $\sigma(a^3F_2$: $VCH_2^+)$ starts to rise at its E_{cm}-threshold of 0.1 ± 0.1 eV, and reaches the peak value of 2.7 Å^2 at $E_{cm} \approx$ 0.8 eV. Above 0.8 eV, $\sigma(a^3F_2$: $VCH_2^+)$ decreases rapidly down to zero at $E_{cm} \approx$ 5.0 eV. Similarly, $\sigma(a^5F_1$: $VCH_2^+)$ [$\sigma(a^5D_0$: $VCH_2^+)$] reaches the peak value of 0.01 Å^2 at $E_{cm} \approx$ 2.0 eV [0.02 Å^2 at $E_{cm} \approx$ 2.5 eV], and decreases quickly down to zero at $E_{cm} \approx$ 5.0 eV. The decrease down to zero at high E_{cm} values could be attributed to the dissociation of excited VCH_2^+ ions, as well as the CID of CH_4, as shown in reaction (4), but these processes occur at higher energies. Rather, as previously described,[19] it can be seen that the peaks in the VCH_2^+ cross sections match the onsets of $VH^+ + CH_3$ formation. As the latter channel can be formed by simple bond cleavage from an $H–V^+–CH_3$ intermediate, whereas dehydrogenation is entropically more difficult, competition between these channels explains the decline in the $VCH_2^+ + H_2$ cross sections. Another reaction involving the formation of VCH_2^+ at high E_{cm} values is shown in reaction (5). However, because of the high endothermicity of 5.7 eV, the occurrence of this reaction channel is expected to have very low probability.

$$V^+(a^5D_0) + CH_4(X^1A_1) \rightarrow VCH_2^+(X^3A_1) + H(^2S_{1/2}) + H(^2S_{1/2})$$
$$E_0 = 5.7 \pm 0.1 \text{ eV} \qquad (5)$$

The $\sigma(VCH_3^+)$ reaction channels are also endothermic, as shown in Fig. 2(g) and (h). Due to the very low reactivity for this reaction channel, only $\sigma(a^3F_2$: $VCH_3^+)$ and $\sigma(a^5D_0$: $VCH_3^+)$ have been detected. Attempts were made to measure $\sigma(a^5F_1$: $VCH_3^+)$ in the E_{cm} range 0.1 to 10.0 eV, but it was observed that the product VCH_3^+ ion signal was below the detection limit when the reactant V^+ ions were prepared in the a^5F_1 state. In addition, for the same reason, the $\sigma(a^5D_0$: $VCH_3^+)$ curve was only measured with very crude E_{cm} step size of 1.0 eV; and the peak value is observed as $\approx$0.007 Å^2 at E_{cm} = 5.0 eV. As the highest cross section among the three, $\sigma(a^3F_2$: $VCH_3^+)$ has an E_{cm}-threshold of E_{cm} = 0.7 ± 0.1 eV and reaches a peak value of 0.08 Å^2 near E_{cm} = 2.7 eV. A flat profile for $\sigma(a^3F_2$: $VCH_3^+)$ is observed at E_{cm} = 0.7 to 1.3 eV. Above 1.3 eV, $\sigma(a^3F_2$: $VCH_3^+)$ starts to increase exponentially, which may indicate the formation of a new reaction channel involving VCH_3^+ populated in an excited state. After reaching the peak value, $\sigma(a^3F_2$: $VCH_3^+)$ decreases rapidly to zero near E_{cm} = 4.0 eV. Similar to $\sigma(VCH_2^+)$, the decay of $\sigma(VCH_3^+)$ can be related to the further dissociation of primary excited VCH_3^+ product ions.

(d) Spin–orbit *J*-state effects

To our best knowledge, no experimental σ measurements for this reaction system with V^+ ion prepared in single J states have previously been reported. The main reason for this challenge can be attributed to the lack of general experimental schemes for the preparation of TM cations in the selected J states. From the point of view of fundamental research, unravelling the J-state effects in chemical reactions involving TM cations is closely related to understanding the roles played by different kinds of angular momenta: spin (S), orbital angular momentum (L), and the total angular momentum (J) arising from the spin–orbit coupling.

In this work, by preparing reactant V^+ ions in single J states, the J-state effects have been examined for the $V^+ + CH_4$ reaction. The comparisons of $\sigma(a^3F_J$: $VH^+, J = 2$ *versus* 3), $\sigma(a^5F_J$: $VH^+, J = 1$ *versus* 2), $\sigma(a^5D_J$: $VH^+, J = 0$ *versus* 2), $\sigma(a^3F_J$: $VCH_2^+, J = 2$ *versus* 3), $\sigma(a^5F_J$:

VCH_2^+, J = 1 *versus* 2), $\sigma(a^5D_J$: VCH_2^+, J = 0 *versus* 2), $\sigma(a^3F_J$: VCH_3^+, J = 2 *versus* 3), and $\sigma(a^5D_J$: VCH_3^+, J = 0 *versus* 2) are shown in Fig. 4(a)–(h), respectively. There it can be seen that the two corresponding J states exhibit essentially identical σ curves as shown in the figures. These results clearly show that no discernible J-state effects are observed for this $V^+ + CH_4$ reaction system. This conclusion is in agreement with that observed in the recent study of other reaction systems, *i.e.*, $V^+ + CO_2$, and $V^+ + D_2$,[24,26] indicating that the spin–orbit coupling of V^+ is weak in the chemical reaction system of $V^+ + CH_4$.

This observation of Fig. 4(a)–(h) is also consistent with the "weak quintet-to-triplet spin crossing" mechanism. The spin–orbit coupling is known to facilitate the mixing among electronic states of TM cations with different multiplicities.[39,40] Thus, if the spin–orbit coupling is strong enough to mix reaction surfaces with different multiplicities, similar chemical reactivity would be observed for TM cations in electronic states with different multiplicities. However, distinct chemical reactivity is observed in this work when the V^+ ion is prepared in single electronic states with different spins. Therefore, this observation is in accordance with weak spin–orbit interaction, suggesting that electron spin S, not J, of the reactant V^+ ion is the constraining factor in determining the chemical reactivity of the $V^+ + CH_4$ reaction.

It is interesting to note that spin–orbit coupling might have been expected to conserve the total electronic angular momentum J. If this were the case, then the $^5D_0$ level should not couple efficiently with $a^3F_{1,2,3}$, whereas the $a^5D_{1,2}$ levels could. The observation that a^5D_0 and a^5D_2 have essentially identical reactivities suggests that molecular angular momentum allows coupling of surfaces of different J.

(e) Branching ratios

The branching ratios (BR's) of the product channels, $VH^+ + CH_3$, $VCH_2^+ + H_2$, and $VCH_3^+ + H$, of the reaction system $V^+(a^5D_0, a^5F_1$, or $a^3F_2) + CH_4(X^1A_1)$ in the E_{cm} range from 0.1 to 10.0 eV are summarized in Table 1 by comparing the relative product VH^+, VCH_2^+, and VCH_3^+ ion intensities. This comparison reveals that as the E_{cm} is increased, $BR(VH^+)$ increases monotonically from 0% to 100%, while $BR(VCH_2^+)$ shows the opposite trend. Furthermore, the $BR(VCH_3^+)$ values are found to have very small values, which are less than 10%.

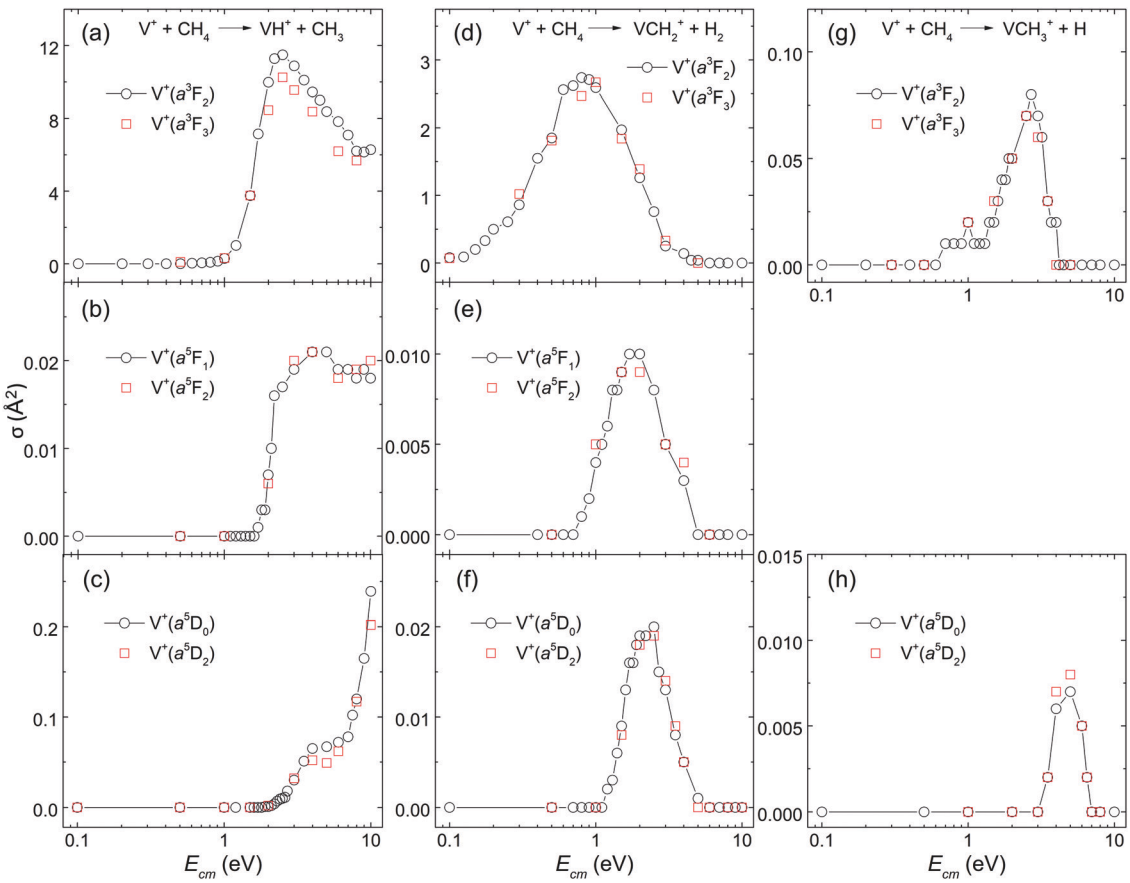

Fig. 4 The spin–orbit J-state effects on $\sigma(VH^+)$, $\sigma(VCH_2^+)$, and $\sigma(VCH_3^+)$ of the reaction system of $V^+(a^3F_{2-3}, a^5F_{1-2}$, and $a^5D_{0,2}) + CH_4$. The comparisons of $\sigma(a^3F_J$: VH^+, J = 2 *vs.* 3), $\sigma(a^5F_J$: VH^+, J = 1 *vs.* 2), $\sigma(a^5D_J$: VH^+, J = 0 *vs.* 2), $\sigma(a^3F_J$: VCH_2^+, J = 2 *vs.* 3), $\sigma(a^5F_J$: VCH_2^+, J = 1 *vs.* 2), $\sigma(a^5D_J$: VCH_2^+, J = 0 *vs.* 2), $\sigma(a^3F_J$: VCH_3^+, J = 2 *vs.* 3), $\sigma(a^5F_J$: VCH_3^+, J = 1 *vs.* 2), and $\sigma(a^5D_J$: VCH_3^+, J = 0 *vs.* 2) are shown in (a), (b), (c), (d), (e), (f), (g), and (h), respectively. These σ curves (arbitrarily selected) for two different J values of individual electronic states are found to be in excellent agreement. This finding clearly indicates negligible J effects for the titled reaction system.

Table 1 The branching ratios (BR's) of $VH^+ + CH_3$, $VCH_2^+ + H_2$, and $VCH_3^+ + H$ reaction product channels for the reaction system of $V^+ + CH_4$ with V^+ prepared in three of its spin–orbit coupled electronic states, a^5D_0, a^5F_1, and a^3F_2 in the E_{cm} range 0.1–10.0 eV. The error limits of ±0.01 represent uncertainties from run-to-run independent measurements[a]

	$V^+(a^5D_0) + CH_4$			$V^+(a^5F_1) + CH_4$			$V^+(a^3F_2) + CH_4$		
E_{cm} (eV)	VH^+	VCH_2^+	VCH_3^+	VH^+	VCH_2^+	VCH_3^+	VH^+	VCH_2^+	VCH_3^+
0.1	—	—	—	—	—	—	0.00	1.00	0.00
0.5	—	—	—	—	—	—	0.00	1.00	0.00
1.0	—	—	—	0.00	1.00	0.00	0.10	0.89	0.01
1.5	0.00	1.00	0.00	0.00	1.00	0.00	0.65	0.34	0.01
2.0	0.05	0.95	0.00	0.41	0.59	0.00	0.88	0.11	0.01
2.5	0.33	0.67	0.00	0.68	0.32	0.00	0.93	0.06	0.01
3.0	0.70	0.30	0.00	0.79	0.21	0.00	0.97	0.02	0.01
4.0	0.85	0.07	0.08	0.87	0.13	0.00	0.98	0.01	0.01
5.0	0.90	0.01	0.09	1.00	0.00	0.00	1.00	0.00	0.00
6.0	0.94	0.00	0.06	1.00	0.00	0.00	1.00	0.00	0.00
7.0	1.00	0.00	0.00	1.00	0.00	0.00	1.00	0.00	0.00
8.0	1.00	0.00	0.00	1.00	0.00	0.00	1.00	0.00	0.00
9.0	1.00	0.00	0.00	1.00	0.00	0.00	1.00	0.00	0.00
10.0	1.00	0.00	0.00	1.00	0.00	0.00	1.00	0.00	0.00

[a] The BRs are listed as zero if they are less than 0.01 and as "—" when all three product channels (or states) have zero σ values.

(f) Simulation of literature σ(SI) curves by using state-selected $\sigma(a^5D_J, a^5F_J,$ and $a^3F_J)$ curves

The previous GIB mass spectrometric experiment was conducted about 33 years ago by the Armentrout group using a hot filament SI ion source at T = 1850–2200 K. The populations of the $V^+(a^5D_J$, a^5F_J, and $a^3F_J)$ states thus generated were assumed to be governed by the Boltzmann distribution.[19] In order to shed light into this assumption, we have performed a simulation of the experimental σ(SI-1850 K) and σ(SI-2200 K) curves. Here, we use the state-selected $\sigma(a^5D_J$, a^5F_J, and $a^3F_J)$ curves obtained in the present study. This simulation also aims to illustrate that hot-band excitations arising from impurity states in σ(SI) measurements can easily prevent the observation of the E_{cm}-thresholds or the E_T values.

As shown below, by taking the linear combination of state-selected $\sigma(a^5D_J$, a^5F_J, and $a^3F_J)$ curves determined in the present PFI-PI measurements, along with weighted Boltzmann populations of these electronic states,[19] we show in Fig. 5(a) and (b) that excellent simulations of the respective experimental σ(SI-1850 K: VH^+) and σ(SI-2200 K: VCH_2^+) curves can be achieved. Fig. 5(a) compares the $\sigma(a^5D_0$: $VH^+)$ curve with the experimental and simulated σ(SI-1850 K: VH^+) and σ(SI-2200 K: VH^+) curves. The V^+ ions produced by thermal SI at 1850–2200 K cannot be in single quantum states. They are expected to populate mostly in the ground a^5D_J cationic state, along with minor populations in the excited a^5F_J and a^3F_J states, which are governed by the Boltzmann distribution. By setting the SI source at 1850 K (2200 K), previous studies assumed that the relative populations of the $V^+(a^5D_J)$, $V^+(a^5F_J)$, and $V^+(a^3F_J)$ states were 0.854, 0.145, and 0.00083 (0.800, 0.191, and 0.0023), respectively.

Since we have obtained detailed quantum state-selected cross section measurements: $\sigma(a^5D_0$: $VH^+)$, $\sigma(a^5F_1$: $VH^+)$, $\sigma(a^3F_2$: $VH^+)$, $\sigma(a^5D_0$: $VCH_2^+)$, $\sigma(a^5F_1$: $VCH_2^+)$, and $\sigma(a^3F_2$: $VCH_2^+)$ curves, we should be able to obtain the simulated σ(SI-1850 K) and σ(SI-2200 K) curves by using these state-selected σ curves and their assumed Boltzmann thermal populations.

In Fig. 5(a), the red solid circle curve represents the $\sigma(a^5D_0$: $VH^+)$ curve obtained from this work, which has been rescaled by a factor of 0.80 in order to emphasize the similarity in the energy dependence. The blue open triangles and green open squares mark the experimental σ(SI-1850 K: VH^+) and σ(SI-2200 K: VH^+) curves, respectively. The orange solid circle curve shows the simulated curve obtained according to the thermal Boltzmann populations at 1850 K calculated as: σ(SI-1850 K: VH^+) = [0.854 × $\sigma(a^5D_0$: $VH^+)$ + 0.145 × $\sigma(a^5F_1$: $VH^+)$ + 0.00083 × $\sigma(a^3F_2$: $VH^+)$] × 0.8. The green solid circle curve shows the simulated σ(SI-2200 K: VH^+) curve, calculated based on the weighted Boltzmann populations as: [0.800 × $\sigma(a^5D_0$: $VH^+)$ + 0.191 × $\sigma(a^5F_1$: $VH^+)$ + 0.0023 × $\sigma(a^3F_2$: $VH^+)$] × 0.8. These simulations thus calculated reveal that $V^+(a^3F_J)$ ions make a significant contribution of broadening of the σ curve involved and to the hot-band tailing structure observed around and below the reaction onset, even though the population of the a^3F_J state is only 0.00083 and 0.0023 at 1850 and 2200 K, respectively. This is because the hot-band contribution of the $\sigma(a^3F_J$: $VH^+)$ curve is hugely amplified by the much higher reactivity of the triplet a^3F_J state compared to that of the quintet states. Thus, hot-band excitations, as in this case, can prevent observation of the true reaction onset.

By comparing the σ(SI-1850 K: VH^+) and σ(SI-2200 K: VH^+) curves with the $\sigma(a^5D_0$: $VH^+)$ curve obtained in this study, we can conclude that the hot-band excitation of the $\sigma(a^5D_0$: $VH^+)$ curve is much reduced; showing that the true 0 K E_T onset, *i.e.*, E_0, is located at a higher E_{cm} still. As shown in Fig. 5(a), the σ(SI) curves observed at 1850 and 2200 K are in excellent agreement with the simulated σ(SI) curves at $E_{cm} \leq 4$ eV, where the simulation of the σ(SI) curves can be obtained by the linear combination of the $\sigma(a^5D_0$: $VH^+)$, $\sigma(a^5F_1$: $VH^+)$, and $\sigma(a^3F_2$: $VH^+)$ curves. The fact that the experimental σ(SI-1850 K: VH^+) and σ(SI-2200 K: VH^+) curves can be well simulated based on the weighted Boltzmann populations is a strong support of the thermal equilibrium assumption. However, the comparison of Fig. 5(a) reveals deviation between the experimental σ(SI) and the simulated curves at $E_{cm} \geq 4$ eV; and the nature of this deviation is not known.

By using similar procedures, we have also obtained excellent simulations for the σ(SI-1850 K: VCH_2^+) and σ(SI-2200 K:

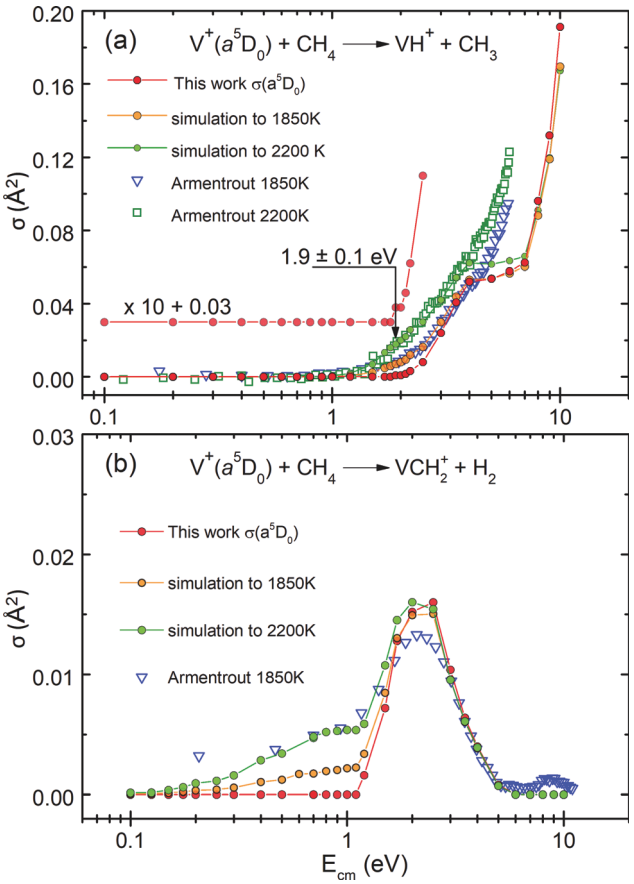

Fig. 5 (a) The red solid circle curve is the $\sigma(a^5D_0: VH^+)$ curve obtained in the present study, which has been rescaled by a factor of 0.80. The blue open triangle and green open square curves are the respective experimental σ(SI-1850 K: VH^+) and σ(SI-2200 K: VH^+) curves. The orange solid circle and green solid circle curves are the respective simulated curves for σ(SI-1850 K: VH^+) and σ(SI-2200 K: VH^+) curves obtained based on the thermal Boltzmann populations of $V^+(a^3F_2, a^5F_1,$ and $a^5D_0)$ states. (b) The red solid circle curve is the $\sigma(a^5D_0: VCH_2^+)$ curve obtained in this work, which has been rescaled by factor of 0.8. The blue open triangle curve is the experimental σ(SI-1850K: VCH_2^+) curve; and the orange solid circle and green solid circle curves are the simulated curves for σ(SI-1850 K: VCH_2^+) and σ(SI-2200 K: VCH_2^+) curves obtained based on the thermal Boltzmann populations of $V^+(a^3F_2, a^5F_1,$ and $a^5D_0)$ states.

VCH_2^+) curves as depicted in Fig. 5(b). Here, the red solid circle curve is the $\sigma(a^5D_0: VCH_2^+)$ curve obtained from this work, whereas the blue open triangle curve is the experimental σ(SI-1850 K: VCH_2^+) curve obtained previously by the Armentrout group. The orange solid circle and green solid circle curves are the simulated curves obtained as the linear combination of the $\sigma(a^5D_0: VCH_2^+)$, $\sigma(a^5F_1: VCH_2^+)$, and $\sigma(a^3F_2: VCH_2^+)$ curves with weighted populations in accordance with the Boltzmann thermal populations observed at T = 1850–2200 K. The simulations of Fig. 5(b) indicate that the hot-tail appearing in the low E_{cm} region is overwhelmingly contributed by the excited triplet $V^+(a^3F_J)$ electronic state in the σ(SI-1850–2200 K: VCH_2^+) measurements.

In addition to validating the thermal equilibrium assumption for the populations of the V^+ electronic states generated by thermal excitations, the excellent simulation observed can also be taken as strong confirmation that the $\sigma(a^5D_0)$, $\sigma(a^5F_1)$, and $\sigma(a^3F_2)$ curves produced in the present PFI-PI study are in single quantum electronic states with 100% purity.

(g) Comparison of present spin–orbit state-selected cross sections with previous results

The fact that the present state-specific results can be used to reproduce the previous data obtained using a surface ionization source also suggests that the assumptions made in this previous work regarding the distribution of electronic states was reasonable. This hypothesis can be further checked by comparing the approximate state-specific cross sections provided by Aristov and Armentrout[19] with the robust determinations obtained here. Fig. 6 compares the present results for $\sigma(a^5D_0: VH^+)$ and $\sigma(a^3F_2: VH^+)$ with those from ref. 19 (taken from Fig. 2 and scaled by the inverse populations: 1/0.854 for the quintet states and 1/0.00083 for the triplets). Clearly, both the shapes and the magnitudes agree well, further validating the accuracy of the present results. A similar comparison of the $\sigma(a^5D_0: VCH_2^+)$ and $\sigma(a^3F_2: VCH_2^+)$s with those from ref. 19 (taken from Fig. 8 directly) find similar agreement in shapes and magnitudes for the quintet states, but the previous data for triplet states is about two times larger in magnitude than the present results, a discrepancy that can be attributed to the extrapolation needed in the previous work. Notably, no reasonable information regarding the a^5F state was obtained in the previous work, which the present study clearly shows is primarily because it is so much less reactive.

(h) Bond dissociation energies of V^+–H, V^+–CH_2, and V^+–CH_3

The D_0 values of V–H^+, V–CH_2^+, and V–CH_3^+ can be derived from E_{cm}-threshold energies or threshold energies of reaction (E_T's) determined in the present experiment. Similar to the derived procedures used in the study of the reaction systems of

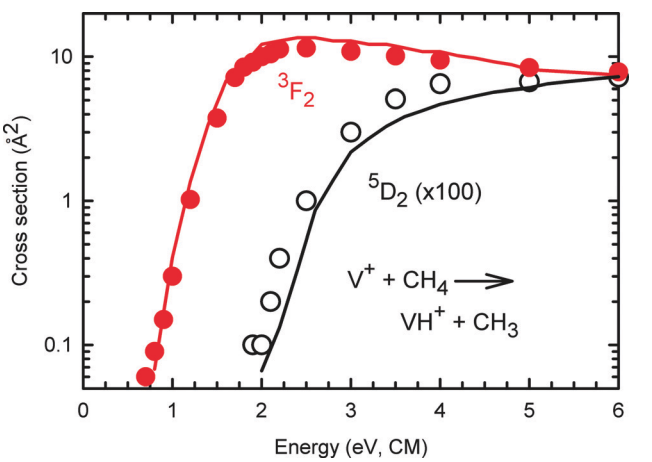

Fig. 6 State-selected $\sigma(a^5D_2: VH^+)$ curve in black circles and $\sigma(a^3F_2: VH^+)$ curve in solid red circles for the reaction channels of $V^+ + CH_4$. The solid lines show the extrapolated state-specific results from ref. 19 for triplet (red) and quintet (black) states. Both data sets for the quintet states have been multiplied by a factor of 100.

$V^+ + D_2$ (CO_2),[24,26] we can show that the D_0 values are related to E_T at $T = 0$ (or E_0) of reactions (1)–(3), given as $E_0(1)$, $E_0(2)$, and $E_0(3)$, in eqn (6)–(8), respectively.

$$D_0(V^+\text{–H}) = D_0(\text{H–CH}_3) - E_0(1) \quad (6)$$

$$D_0(V^+\text{–CH}_2) = D_0(\text{H–CH}_3) + D_0(\text{H–CH}_2) - 2\Delta_f H_0(\text{H}) - E_0(2) \quad (7)$$

$$D_0(V^+\text{–CH}_3) = D_0(\text{H–CH}_3) - E_0(3) \quad (8)$$

Here, $D_0(\text{H–CH}_3)$, $D_0(\text{H–CH}_2)$, and $\Delta_f H_0(\text{H})$ are the 0 K bond dissociation energies of H–CH_3, H–CH_2, and the 0 K heat of formation of H atom [$\Delta_f H_0(\text{H})$], respectively. From available ref. 41 and 42, the values of $D_0(\text{H–CH}_3)$, $D_0(\text{H–CH}_2)$, and $2\Delta_f H_0(\text{H}) = D_0(H_2)$ are known to be 4.482 ± 0.001, 4.739 ± 0.001, and 4.478 ± 0.001 eV, respectively.

As shown in Fig. 2(a)–(c), the E_{cm}-thresholds or E_T values observed for $\sigma(a^3F_2$: $VH^+)$, $\sigma(a^5F_1$: $VH^+)$, and $\sigma(a^5D_0$: $VH^+)$ are 0.6 ± 0.1, 1.7 ± 0.1, and 1.9 ± 0.1 eV, which give the values of bond dissociation energy of VH^+ ($D_0(V^+\text{–H})$) as 2.8 ± 0.1, 2.5 ± 0.1, and 2.6 ± 0.1 eV, respectively. Thus, the averaged value of $D_0(V^+\text{–H})$ can be determined as 2.6 ± 0.2 eV, which is in good agreement with the $D_0(V^+\text{–D})$ value of 2.5 ± 0.2 eV that has been deduced recently in the study of another reaction system of $V^+ + D_2$.[26] Similarly, the $D_0(V^+\text{–CH}_2)$ can be derived as 3.6 ± 0.1, 3.7 ± 0.1, and 3.6 ± 0.1 eV, corresponding to the E_T's of 0.1 ± 0.1, 0.8 ± 0.1, and 1.2 ± 0.1 eV for $\sigma(a^3F_2$: $VCH_2^+)$, $\sigma(a^5F_1$: $VCH_2^+)$, and $\sigma(a^5D_0$: $VCH_2^+)$ in Fig. 2(d)–(f), respectively. Thus, the averaged $D_0(V^+\text{–CH}_2)$ is 3.6 ± 0.2 eV. For $\sigma(VCH_3^+)$ shown in Fig. 2(g) and (h), due to the very low reactivity, only the E_T for $\sigma(a^3F_2$: $VCH_3^+)$ has been determined with sufficiently high quality for reliable bond energy determination. Based on the latter E_T value of 0.7 ± 0.1 eV for $\sigma(a^3F_2$: $VCH_3^+)$, the $D_0(V^+\text{–CH}_3)$ is deduced as 2.7 ± 0.2 eV.

We emphasize that the direct D_0 determination as shown in eqn (6)–(8) requires the E_0 instead of the E_T measurement. The most important thermal energy correction for the conversion of E_T to E_0 measurement is expected to be the thermal energy of reactant CH_4 molecule, in this case. Since the thermal energy for CH_4 has not been properly accounted and corrected for in the above thermochemical analyses and derivation, all the D_0 values deduced above associated with the reaction systems of $V^+ + D_2$ (CO_2, CH_4) are upper bound values, which are found to be higher than the accepted corresponding literature values by ≈0.3–0.5 eV. That is, following the data analysis as given above, we have: $D_0(V^+\text{–H}) \leq 2.6 \pm 0.2$ eV, $D_0(V^+\text{–CH}_2) \leq 3.6 \pm 0.2$ eV, and $D_0(V^+\text{–CH}_3) \leq 2.7 \pm 0.2$ eV.

As pointed out earlier, the shifting of the E_{cm}-threshold positions of $\sigma(VH^+)$, $\sigma(VCH_2^+)$, and $\sigma(VCH_3^+)$ observed, due to the change of the quantum electronic states of the reactant V^+ ions, indicates that the quantum electronic energy can couple with the reaction coordinates in promoting accessible chemical reaction channels, similar to the E_{cm}.

(i) Modelling of kinetic energy distribution due to thermal broadening

Previous studies have shown that, in order to obtain reliable 0 K bond dissociation energies for simple TM-ligated molecules, such as $D_0(V^+\text{–H})$, $D_0(V^+\text{–CH}_2)$, and $D_0(V^+\text{–CH}_3)$, it is necessary to account for the proper correction of thermal energies involved, particularly on the thermal energy associated with the neutral reactant CH_4 molecule in this case. On the basis of the theoretical analysis of Chantry[35] and Lifshitz *et al.*,[43] the Armentrout group has developed a simulation program for the determination of the threshold energy of reaction E_0 and the kinetic energy distribution by fitting the experimental σ curves based on the semi-empirical modified line-of-centers (MLOC) model as shown in eqn (9).[44,45]

$$\sigma_0(E_{cm}) = \sum g_i(E_{cm} + E_{el} + E_i - E_0)^n/E_{cm} \quad (9)$$

Here σ_0 is an empirical scaling parameter, E_{el} is the electronic energy of the specific spin–orbit level of V^+, E_i is the internal energy of the methane having rovibrational states i with population g_i, $\sum g_i = 1$, at the reaction cell temperature of 298 K, and n is an empirical fitting parameter. Before comparison with the experimental data, this model was convoluted over the kinetic energy distributions of the reactants.[35,43,46] In the present study, the value of n was fixed and the σ_0 and E_0 parameters were optimized by a nonlinear least-square method for best reproduction of the experimental reaction cross sections. As an example, we show in Fig. 6 typical fits achieved to the state-selected $\sigma(a^5D_2$ and a^3F_2: $VH^+)$ curves; and in Fig. 7 state-selected $\sigma(a^5D_2$: $VCH_2^+)$ curve in black circles, $\sigma(a^5F_1$: $VCH_2^+)$ curve in solid blue circles, and $\sigma(a^3F_2$: $VCH_2^+)$ curve in solid red circles based on the semi-empirical MLOC model. Uncertainties in the modeling parameters were obtained *via* analyses using a range of acceptable n values and include the absolute uncertainty in the center-of-mass energy scale. At higher energies, the σ curve can decline because the product ion can dissociate or because of competition with other channels. This behavior was reproduced using a model detailed elsewhere that includes conservation of angular momentum along with an

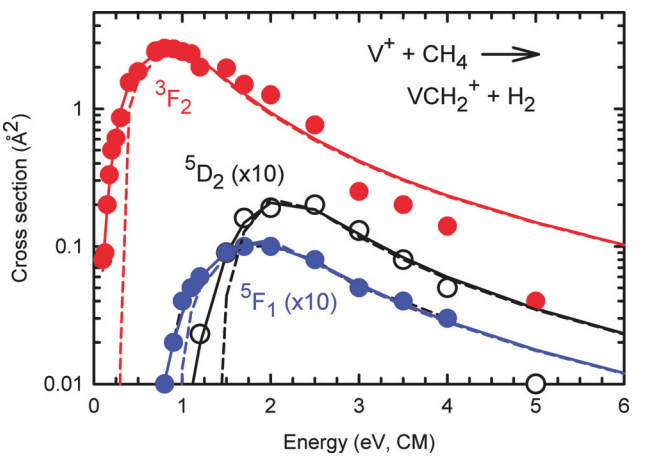

Fig. 7 State-selected $\sigma(a^5D_2$: $VCH_2^+)$ curve in black circles, $\sigma(a^5F_1$: $VCH_2^+)$ curve in solid blue circles, and $\sigma(a^3F_2$: $VCH_2^+)$ curve in solid red circles for the reaction channels of $V^+ + CH_4$. The solid (dashed) lines show the fits based on the empirical modified line-of-centers (MLOC) models for each data set including (excluding) convolution with the kinetic and internal energy distributions of the reactants. The data and models for the two quintet states have been multiplied by a factor of 10.

empirical parameter (p) that controls how fast the decline occurs.[47] Eqn (9) is multiplied by P_D, the probability of product ion dissociation (competition), which is controlled by two parameters, p, similar to n but limited to integral values, and E_D, the energy where the product ion begins to dissociate (or competition ensues). These two parameters were optimized for best reproduction of the experimental data without affecting the threshold determinations.

Threshold energies of reaction can be converted to thermochemical parameters and properties using eqn (6)–(8). This assumes that the thresholds correspond to the asymptotic product energies, such that there are no reverse activation barriers. This result is expected in the present system for all reactions. As reported above, relevant literature thermochemistry includes the active thermochemical table (aTcT) values of $D_0(CH_2–H_2)$ = 4.743 eV and $D_0(CH_3–H)$ = 4.482 eV.[41,42]

To extract meaningful thermochemistry from the kinetic energy dependent cross sections, they were modeled using eqn (9), which explicitly includes all sources of energy after convolution with the kinetic energy distributions of both reactants. Because the density of data points is relatively low, it is not possible to allow all parameters in this equation to vary freely, hence the modeling results from Aristov and Armentrout[17] were used as a guide for selecting the value of n coupled with whether the cross section was adequately reproduced. In all cases, the simple line-of-centers (LOC) model where n = 1 reproduces the data well. The optimized parameters used are listed in Table 2. For the formation of $VCH_2^+ + H_2$, the thresholds for the a^5F_1 and a^3F_2 excited levels are smaller than that for the a^5D_0 ground level by 0.46 ± 0.09 and 1.11 ± 0.09 eV, in reasonable agreement with the excitation energies of 0.32 and 1.07 eV.[38] Likewise, for the $VH^+ + CH_3$ channel, the thresholds shift by 0.24 ± 0.12 and 1.06 ± 0.12 eV, respectively. In both cases, the thresholds obtained provide weighted average bond dissociation energies of $D_0(V^+–CH_2)$ = 3.40 ± 0.14 eV and $D_0(V^+–H)$ = 2.02 ± 0.09 eV (where the uncertainties are two standard deviations of the mean). The former value can be compared to that obtained by Aristov and Armentrout of 3.30 ± 0.06 eV (from reactions of V^+ with C_2H_{2p})[48] and by Aristov and Armentrout of 3.47 ± 0.13 eV (from reaction of V^+ with CH_4),[19] both at 298 K. The latter result was later adjusted to a 0 K value of 3.37 ± 0.06 eV by Armentrout and Kickel.[49] Likewise, the value for $D_0(V^+–H)$ obtained here agrees nicely with that obtained by Elkind and Armentrout, 2.05 ± 0.06 eV (reaction of $V^+ + H_2$ and D_2),[23] and with that obtained by combining these earlier results with state-selected experiments on the reaction $V^+ + D_2$ similar to the present study, 2.07 ± 0.09 eV.[27]

In contrast to the results for VCH_2^+ and VH^+ products, only the thresholds obtained using the LOC model for $VCH_3^+ + H$ reaction from the a^3F_2 state yields a reliable threshold that corresponds to $D_0(V^+–CH_3)$ = 2.07 ± 0.09 eV. This value agrees with that previously obtained by Aristov and Armentrout[48] after being adjusted to 0 K by Armentrout and Kickel, 2.00 ± 0.07 eV.[49] Furthermore, it is similar to the value obtained here for $D_0(V^+–H)$. As discussed by Armentrout and Kickel,[49] this similarity, which holds for all first-row transition metal cations, is expected because both molecules involve single covalent bonds to V^+.

Table 2 Modified line-of-centers models eqn (9) of state-selected data for reaction of V^+ with methane[a]

Product	State	σ_0	N	E_0 (eV)	$D_0(V^+–X)$
VCH_2^+	$V^+(a^5D_0)$	0.075 (0.005)	1.0 (0.1)	1.41 (0.08)	3.33 (0.08)
	$V^+(a^5F_1)$	0.025 (0.004)	1.0 (0.1)	0.95 (0.06)	3.47 (0.06)
	$V^+(a^3F_2)$	3.9 (0.2)	1.0 (0.1)	0.30 (0.06)	3.37 (0.06)
VH^+	$V^+(a^5D_0)$	0.14 (0.03)	0.9 (0.2)	2.42 (0.10)	2.06 (0.10)
	$V^+(a^5F_1)$	0.22 (0.02)	1.0 (0.1)	2.18 (0.06)	1.98 (0.06)
	$V^+(a^3F_2)$	28.5 (0.5)	1.0 (0.1)	1.36 (0.06)	2.05 (0.06)
VCH_3^+	$V^+(a^3F_2)$	0.15 (0.1)	1.0 (0.1)	1.34 (0.09)	2.07 (0.09)

[a] Uncertainties (one standard deviation) in parentheses.

(j) E_T-threshold energy of reaction approach for bond energy measurements

As pointed out above, the effect of the thermal motion of neutral gaseous molecules in the reaction cell contributes significant uncertainty of collision energy. Chantry[35] has shown that the kinetic energy distribution at E_{cm} has the full-width-at-half-maximum of

$$W_{1/2} = \sqrt{[11.1 \times \gamma kT \times E_{cm}]}. \quad (10)$$

Here, T = 298 K of neutral CH_4 gas, k is the Boltzmann constant, and $\gamma = [m^+/(M + m^+)]$, where m^+ and M are the masses of reactant ion and reactant neutral, respectively. For the reaction of $V^+ + CH_4$, m^+ = 51 amu, M = 16 amu, and γ = 51/67. Because of the broadening effect from the thermal kinetic motion of CH_4, the E_T value should be down-shifted from the true onset of reaction E_0. At $E_{cm} = E_0$ (the true reaction onset), the kinetic energy spread is $W_{1/2} = 2\Delta E = \sqrt{[11.1 \times \gamma kT \times E_0]} = \sqrt{[0.217 \times E_0]}$. Assuming the E_T onset is observed when CH_4 moves against V^+ with a kinetic energy lower by the half maximum of the distribution, then $E_0 = E_T + \Delta E$. This yields eqn (11) and (12), which allow the calculation of ΔE from E_T.

$$W_{1/2} = \sqrt{[0.217 \times E_0]} = \sqrt{[0.217 \times (E_T + \Delta E)]} = 2\Delta E \quad (11)$$

$$4\Delta E^2 - 0.217\ \Delta E - (0.217E_T) = 0 \quad (12)$$

By taking into account the ΔE term, which can be deduced from eqn (10)–(12) based on the thermal broadening effect, we have deduced the D_0 values of V^+–H, V^+–CH_2, and V^+–CH_3 using eqn (6)–(8). The D_0 and E_0 values obtained based on E_T-threshold energy measurements are compared in Table 3 with the results obtained based on the simulation approach. As shown in the table, excellent agreement is observed between the results of the two experimental approaches for VCH_2^+, whereas the values for VH^+ and VCH_3^+ are outside the combined uncertainties. Considering that the simulation approach is a more precise treatment and includes the entire distributions of energies available, the simulation approach should be the method of choice. Nevertheless, the E_T-threshold approach has the advantage of being straightforward with clearly tractable physical insight. When combined with high level *ab initio* calculations, both the E_T-threshold and the simulation approaches can be profitable for the study of energetics and bonding

Table 3 Comparison of E_0 and D_0 values obtained based on the simulation of state-selected $\sigma(VH^+)$, $\sigma(VCH_2^+)$, and $\sigma(VCH_3^+)$ curves with those observed by E_T-threshold measurements for the reaction system of $V^+(a^3F_2, a^5F_1, \text{and } a^5D_0) + CH_4$[a]

		Simulation approach		E_T-threshold approach	
Product	State	E_0 (eV)	$D_0(V^+–X)$ (eV)	E_0 (eV)	$D_0(V^+–X)$ (eV)
VH^+	$V^+(a^5D_0)$	2.42 (0.10)	2.06 (0.10)	2.25 (0.17)	2.23 (0.17)
	$V^+(a^5F_1)$	2.18 (0.06)	1.98 (0.06)	2.03 (0.17)	2.13 (0.17)
	$V^+(a^3F_2)$	1.36 (0.06)	2.05 (0.06)	0.81 (0.10)	2.60 (0.10)
			2.02 (0.05)[b]		2.43 (0.26)[b]
			2.05 (0.06)[cd]		
			2.07 (0.09)[e]		
VCH_2^+	$V^+(a^5D_0)$	1.41 (0.08)	3.33 (0.08)	1.48 (0.14)	3.26 (0.14)
	$V^+(a^5F_1)$	0.95 (0.06)	3.47 (0.06)	1.01 (0.12)	3.41 (0.14)
	$V^+(a^3F_2)$	0.30 (0.06)	3.37 (0.06)	0.21 (0.10)	3.47 (0.10)
			3.40 (0.07)[b]		3.40 (0.11)[b]
			3.37 (0.06)[d]		
VCH_3^+	$V^+(a^3F_2)$	1.34 (0.09)	2.07 (0.09)	0.92 (0.10)	2.48 (0.10)
			2.00 (0.07)[d]		

[a] Uncertainties (one standard deviation) in parentheses. [b] Weighted averages of $D_0(V^+–X)$, X = H and CH_2. [c] Ref. 23. [d] Ref. 49. [e] Ref. 27.

properties of TM-ligated chemical species, many of which are still unavailable in the literatures.

IV. Conclusions

In this work, the $\sigma(VH^+)$, $\sigma(VCH_2^+)$, and $\sigma(VCH_3^+)$ of the reaction system $V^+(a^5D_0, a^5F_1, \text{and } a^3F_2) + CH_4(X^1A_1)$ have been measured in the E_{cm} range from 0.1 to 10.0 eV, by coupling a novel two-color VIS-UV laser PFI-PI V^+ ion source with a DQDO ion–molecule reaction apparatus. Both quantum spin–orbit electronic state and E_{cm} effects on chemical reactivity for this reaction system have been examined in detail. The triplet $V^+(a^3F_J)$ ion is found to exhibit much higher chemical reactivity than that of the two quintet ions, $V^+(a^5D_J)$ and $V^+(a^5F_J)$, confirming the more qualitative conclusions of previous studies.[19] Without a detailed theoretical examination of the reaction dynamics of the titled reaction system, this observation is tentatively interpreted by a weak quintet-to-triplet spin crossing mechanism, favoring dominantly the conservation of total electron spin. The preference for the conservation of total electron spin may promote the formation of an inserted intermediate, $[HV^+CH_3]$, which can thus enhance the reactivity of the triplet $V^+(a^3F_J)$ ion. Although the electronic energy of $V^+(a^5F_J)$ ion is 0.3 eV higher than that of the $V^+(a^5D_J)$ ion, the reactivity of the $V^+(a^5F_J)$ ion is found to be lower than that of the $V^+(a^5D_J)$ ion, indicating that chemical reactivity of V^+ ions is governed by quantum state effects rather than energy effects.

The E_{cm}-thresholds of $\sigma(VH^+)$, $\sigma(VCH_2^+)$, and $\sigma(VCH_3^+)$ for V^+ prepared in the a^5D_0, a^5F_1, or a^3F_2 states have been determined except that for $\sigma(a^5F_J: VCH_3^+)$. From the E_T-threshold energies of reaction measurements, the upper limits for $D_0(V^+–H)$, $D_0(V^+–CH_2)$, and $D_0(V^+–CH_3)$ values have been deduced. By properly accounting for the thermal kinetic energy distribution primarily resulting from the thermal broadening effects of the neutral reactant CH_4 molecule, we have obtained reliable D_0 values for these V^+-ligated molecular ions. The differences of E_{cm}-thresholds observed are consistent with the electronic state energy levels of reactant V^+ ions, indicating that quantum electronic energies of V^+ ions similar to E_{cm}, can couple effectively with the reaction coordinates of the $V^+ + CH_4$ reaction system. No J effect has been observed, which may mean that the spin–orbit coupling of $V^+(a^5D_0, a^5F_1, \text{or } a^3F_2)$ of V^+ ion is weak and J is not a constraining factor to this reaction system. The weak spin–orbit coupling is expected to lower the mixing of electronic states with different multiplicities (or spins), which is in accordance with the distinct differences of observed chemical reactivity for V^+ ions prepared in electronics states with different spins. Detailed BR's have also been obtained as a function of E_{cm} and electronic states of V^+ ion, together with quantum state-selected σ's, can serve as experimental benchmarks for state-of-the-art theoretical calculations of model reaction systems. The much higher reactivity and product selectivity of the $V^+(a^3F_J) + CH_4$ reaction leading to H_2 formation observed in this work may provide valuable insight into designing more effective catalytic pathways for CH_4 activation. This and the recent V^+ state-selected ion–molecule reaction experiments have shown that the E_T-threshold energy and σ curve measurements represent a fruitful experimental and theoretical research area for the study of chemical bonding between TM cations and ligands.

Conflicts of interest

There are no conflicts to declare.

Acknowledgements

This work is supported by the National Science Foundation, Grant CHE-1763319 (CYN) and CHE-1664618 (PBA). CYN is also grateful to Dr Huie Tarng Liou for his generous donation of research support for the Ng Laboratory.

References

1 S. A. Montzka, E. J. Dlugokencky and J. H. Butler, *Nature*, 2011, **476**, 43–50.
2 C. R. Webster, P. R. Mahaffy, S. K. Atreya, G. J. Flesch, M. A. Mischna, P. Y. Meslin, K. A. Farley, P. G. Conrad,

L. E. Christensen, A. A. Pavlov, J. Martín-Torres, M. P. Zorzano, T. H. McConnochie, T. Owen, J. L. Eigenbrode, D. P. Glavin, A. Steele, C. A. Malespin, P. D. Archer, Jr., B. Sutter, P. Coll, C. Freissinet, C. P. McKay, J. E. Moores, S. P. Schwenzer, J. C. Bridges, R. Navarro-Gonzalez, R. Gellert and M. T. Lemmon, *Science*, 2015, **347**, 415–417.

3 S. K. Atreya, E. Y. Adams, H. B. Niemann, J. E. Demick-Montelara, T. C. Owen, M. Fulchignoni, F. Ferri and E. H. Wilson, *Planet. Space Sci.*, 2006, **54**, 1177–1187.

4 C. J. Bennett, C. S. Jamieson, Y. Osamura and R. I. Kaiser, *Astrophys. J.*, 2006, **653**, 792–811.

5 O. Mousis, E. Chassefiere, N. G. Holm, A. Bouquet, J. H. Waite, W. D. Geppert, S. Picaud, Y. Aikawa, M. Ali-Dib, J.-L. Charlou and P. Rousselot, *Astrobiology*, 2015, **15**, 308–326.

6 C. Mesters, *Annu. Rev. Chem. Biomol. Eng.*, 2016, **7**, 223–238.

7 A. Bard, G. M. Whitesides, R. N. Zare and F. W. McLafferty, *Acc. Chem. Res.*, 1995, **28**, 91.

8 H. Schwarz, *Angew. Chem., Int. Ed.*, 2011, **50**, 10096–10115.

9 L. Barelli, G. Bidini, F. Gallorini and S. Servili, *Energy*, 2008, **33**, 554–570.

10 M. E. Dry, *Catal. Today*, 2002, **71**, 227–241.

11 H. Jahangiri, J. Bennett, P. Mahjoubi, K. Wilson and S. Gu, *Catal. Sci. Technol.*, 2014, **4**, 2210–2229.

12 J. C. Weisshaar, *Acc. Chem. Res.*, 1993, **26**, 213–219.

13 J. Roithová and D. Schröder, *Chem. Rev.*, 2010, **110**, 1170–1211.

14 P. B. Armentrout and J. L. Beauchamp, *J. Am. Chem. Soc.*, 1981, **103**, 784–791.

15 P. B. Armentrout and J. L. Beauchamp, *Acc. Chem. Res.*, 1989, **22**, 315–321.

16 J. Allison, R. B. Freas and D. P. Ridge, *J. Am. Chem. Soc.*, 1979, **101**, 1332–1333.

17 A. Shayesteh, V. V. Lavrov, G. K. Koyanagi and D. K. Bohme, *J. Phys. Chem. A*, 2009, **113**, 5602–5611.

18 D. Schröder and H. Schwarz, *Proc. Natl. Acad. Sci. U. S. A.*, 2008, **105**, 18114–18119.

19 N. Aristov and P. B. Armentrout, *J. Phys. Chem.*, 1987, **91**, 6178–6188.

20 T. Hayes, D. Bellert, T. Buthelezi and P. J. Brucat, *Chem. Phys. Lett.*, 1997, **264**, 220–224.

21 E. Sicilia and N. Russo, *J. Am. Chem. Soc.*, 2002, **124**, 1471–1480.

22 E. U. Condon and G. H. Shortley, *The Theory of Atomic Spectra*, Cambridge University Press, 1951.

23 J. L. Elkind and P. B. Armentrout, *J. Phys. Chem.*, 1985, **89**, 5626–5636.

24 Y. C. Chang, Y. Xu and C.-Y. Ng, *Phys. Chem. Chem. Phys.*, 2019, **21**, 6868–6877.

25 Y. C. Chang, B. Xiong, Y. Xu and C.-Y. Ng, *J. Phys. Chem. A*, 2019, **123**, 2310–2319.

26 Y. Xu, Y.-C. Chang and C.-Y. Ng, *J. Phys. Chem. A*, 2019, **123**, 5937–5944.

27 P. B. Armentrout, Y.-C. Chang and C.-Y. Ng, *J. Phys. Chem. A*, 2020, **124**(26), 5306–5313.

28 M. R. Sievers and P. B. Armentrout, *J. Chem. Phys.*, 1995, **102**, 754–762.

29 Y. C. Chang, Y. Xu, B. Xiong and C.-Y. Ng, *Mol. Phys.*, 2020, 1–11.

30 Y. C. Chang, H. Xu, Y. Xu, Z. Lu, Y.-H. Chiu, D. J. Levandier and C. Y. Ng, *J. Chem. Phys.*, 2011, **134**, 201105.

31 Y. C. Chang, Y. Xu, Z. Lu, H. Xu and C. Y. Ng, *J. Chem. Phys.*, 2012, **137**, 104202.

32 N. R. Daly, *Rev. Sci. Instrum.*, 1960, **31**, 264–267.

33 Y. Xu, B. Xiong, Y. C. Chang and C.-Y. Ng, *Astrophys. J.*, 2018, **861**, 17.

34 Y. Xu, B. Xiong, Y. C. Chang and C.-Y. Ng, *J. Phys. Chem. A*, 2018, **122**, 6491–6499.

35 P. J. Chantry, *J. Chem. Phys.*, 1971, **55**, 2746–2759.

36 G. Friedlander, J. W. Kennedy and E. S. Macias, *Nuclear and radiochemistry*, John Wiley & Sons, 1981.

37 J. E. Sansonetti and W. C. Martin, *J. Phys. Chem. Ref. Data*, 2005, **34**, 1559–2259.

38 A. Kramida, Y. Ralchenko, J. Reader and N. A. Team, National Institute of Standards and Technology, Gaithersburg, MD, 2012.

39 H. Schwarz, *Int. J. Mass Spectrom.*, 2004, **237**, 75–105.

40 J. N. Harvey, *Phys. Chem. Chem. Phys.*, 2007, **9**, 331–343.

41 B. Ruscic, R. E. Pinzon, M. L. Morton, G. von Laszevski, S. J. Bittner, S. G. Nijsure, K. A. Amin, M. Minkoff and A. F. Wagner, *J. Phys. Chem. A*, 2004, **108**, 9979–9997.

42 B. Ruscic and D. H. Bross, Active Thermochemical Tables (ATcT) values based on ver. 1.122g of the Thermochemical Network, available at ATcT.anl.gov, accessed 4/29/20.

43 C. Lifshitz, R. L. C. Wu, T. O. Tiernan and D. T. Terwilliger, *J. Chem. Phys.*, 1978, **68**, 247–260.

44 R. H. Schultz, K. C. Crellin and P. Armentrout, *J. Am. Chem. Soc.*, 1991, **113**, 8590–8601.

45 N. Dalleska, K. Honma, L. Sunderlin and P. Armentrout, *J. Am. Chem. Soc.*, 1994, **116**, 3519–3528.

46 K. M. Ervin and P. B. Armentrout, *J. Chem. Phys.*, 1985, **83**, 166–189.

47 M. E. Weber, J. L. Elkind and P. B. Armentrout, *J. Chem. Phys.*, 1986, **84**, 1521–1529.

48 N. Aristov and P. B. Armentrout, *J. Am. Chem. Soc.*, 1986, **108**, 1806–1819.

49 P. B. Armentrout and B. L. Kickel, in *Organometallic Ion Chemistry*, ed. B. S. Freiser, Kluwer, Dordrecht, 1996, pp. 1–45.

